Influences of microparticle radius and microchannel height on SSAW-based acoustophoretic aggregation

Jing Dong[1], Dongfang Liang[1,*], Xin Yang[2], Chao Sun[3]

[1] Department of Engineering, University of Cambridge, Cambridge CB2 1PZ, UK

[2] Department of Electrical and Electronic Engineering, School of Engineering, Cardiff University, Cardiff CF24 3AA, UK

[3] School of Life Sciences, Northwestern Polytechnical University, 710129, P.R. China

* Corresponding author, dl359@cam.ac.uk

Abstract

The use of acoustic waves for microfluidic aggregation has become widespread in chemistry, biology and medicine. Although numerous experimental and analytical studies have been undertaken to study the acoustophoretic aggregation mechanisms, few studies have been conducted to optimise the device design. This paper presents a numerical investigation of the acoustophoresis of microparticles suspended in compressible liquid. The wall of the rectangular microchannel is made of Polydimethylsiloxane (PDMS), and Standing Surface Acoustic Waves (SSAW) are introduced into the channel from the bottom wall. First, the relative amplitude of the acoustic radiation force and the viscous drag force is evaluated for particles of different radii ranging from 0.1μm to 15μm. Only when the particle size is larger than a critical value can the particles accumulate at acoustic pressure nodes (PNs). The efficiency of the particle accumulation depends on the microchannel height, so an extensive parametric study is then undertaken to identify the optimum microchannel height. The optimum height, when normalised by the acoustic wavelength, is found to be between 0.57-0.82. These findings provide insights into the design of acoustophoretic devices.

Key words: microparticle aggregation; microfluidics; acoustofluidics; acoustophoresis; microchannels

1. Introduction

There has been growing interest in non-invasive manipulation of micro-objects and fluids in biophysical, biochemical and biomedical fields in recent years [1-4]. Among the various methods, those based on Standing Surface Acoustic Waves (SSAW) have been intensively used due to their advantages, such as excellent biocompatibility, label-free operation, contactless manipulation, simplicity and affordability [5-8].

In an SSAW-based device, particle manipulation is achieved by generating a standing acoustic field inside a microfluidic channel. To establish a SSAW field, two pairs of interdigitated transducers (IDTs) are driven by alternating current (AC) signals and are placed on the surface of a piezoelectric substrate to generate two SAWs propagating in opposite directions. The interference between these two SAWs of the same frequency and amplitude forms SSAWs at the bottom of the microchannel. The SSAW leaks into the overlying fluid, and the acoustic field perturbs the fluid and the suspended particles. When a particle is suspended in the fluid, it experiences an acoustic radiation force (F_{rad}) induced by the scattering of the acoustic waves and a viscous drag force (F_{drag}) arising from acoustic streaming [9,10]. When the width of the device is equal to the acoustic wavelength, suspended solid particles will move towards the centreline and the two sidewalls where pressure nodes (PNs) are located.

The SSAW fields can be used to manipulate microparticles of different properties because the acoustophoretic response is dependent on the particle size, density and compressibility. There have been numerous experimental studies based on this concept [11-16]. Recently, there have also been extensive theoretical and numerical studies of the SSAW-based systems, which are valuable for gaining insights into the detailed particle motion and for achieving the optimised design. Muller et al.[17] built a FEM model using a comprehensive perturbation method to study the transient motion of microparticles inside the acoustofluidic channel. Nama et al.[18] extended Muller's model by specifying impedance boundary conditions to represent wave absorption at

three PDMS walls and specifying displacement boundary conditions to represent acoustic actuation at the bottom surface. Ni et al.[19] illustrated observable effects of shear waves through the solid PDMS wall on the acoustic streaming and microparticle motion, and suggested that the damping effect should be taken into account when estimating the pressure fields in simplified models. Skov et al.[20] carried out three-dimensional (3D) simulations of a SAW-based system and considered both the electromechanical and acoustic displacement effects. Hsu and Chao[21] developed a full-wave FEM model that includes the piezoelectric substrate with interdigitated electrodes, the soft elastic solid walls of the channel and the enclosed liquid-particle mixture.

This paper focuses on two aspects of the SSAW-based system, which have not been fully understood from the past research. One is the effect of the particle size on the relative magnitude of the acoustic radiation force and viscous drag force. The other is the optimum height of the SSAW-based device, which greatly influences the aggregation efficiency. In this work, the finite element method is used to model the acoustophoresis of microparticles in an SSAW-driven microchannel made of PDMS walls. The microparticles are suspended in an isentropic compressible liquid inside the channel. The fluid motion is governed by the continuity and Navier-Stokes equations. The perturbation theory is used to numerically solve these governing equations. The first-order solution corresponds to the periodic oscillations, while the second-order solution is related to the acoustic streaming field. The period-averaged forces, including the acoustic radiation force and viscous drag force, act on solid particles to drive their motion. To validate this numerical model, three past case studies are reproduced, including those in Nama et al. [18], Sun et al. [16] and Mikhaylov et al. [22]. Subsequently, the influences of the particle size and the microchannel height are studied systematically. These findings can provide a better understanding of the transition from the radiation-dominated motion to streaming-dominated motion and of the optimisation of the SSAW-based device.

2. Mathematical Model

2.1 Governing equations of fluid

The motion of a viscous weakly-compressible fluid is governed by the principles of mass conservation and momentum conservation [23]. Because of the time scale disparity between the acoustic oscillation and particle motion, the acoustofluidic motion induced by harmonic forcing can be decomposed into two parts: a periodic component with the same period as the acoustic actuation and a second-order component with a non-zero time-averaged motion. Nyborg's perturbation technique can be employed to write the fluid velocity, pressure and density into the following expressions [24]:

$$\boldsymbol{v} = \boldsymbol{v_0} + \boldsymbol{v_1} + \boldsymbol{v_2} + \ldots \tag{1a}$$

$$p = p_0 + p_1 + p_2 + \ldots \tag{1b}$$

$$\rho = \rho_0 + \rho_1 + \rho_2 + \ldots \tag{1c}$$

where $\boldsymbol{v}$, p and ρ are the fluid velocity vector, fluid pressure and mass density, respectively, the subscripts 0, 1 and 2 represent the zeroth-order (or hydrostatic), first-order and second-order components, respectively.

2.2 First-order and second-order equations

By neglecting high-order terms, the following first-order equations can be derived, which specify the harmonic component of fluid response to the imposed acoustic oscillation.

$$\frac{\partial \rho_1}{\partial t} = -\rho_0 \nabla \cdot \boldsymbol{v_1} \tag{2a}$$

$$\rho_0 \frac{\partial \boldsymbol{v_1}}{\partial t} = -\nabla p_1 + \mu \nabla^2 \boldsymbol{v_1} + \left(\mu_b + \frac{\mu}{3}\right) \nabla(\nabla \cdot \boldsymbol{v_1}) \tag{2b}$$

where μ and μ_b are shear and bulk viscosity coefficients of the fluid, respectively. Similarly, the time-averaged second-order equation can be derived as [17, 23]:

$$-\nabla \cdot \langle \rho_1 \cdot \boldsymbol{v_1} \rangle = \rho_0 \nabla \cdot \langle \boldsymbol{v_2} \rangle \tag{3a}$$

$$\langle \rho_1 \frac{\partial \boldsymbol{v_1}}{\partial t} \rangle + \rho_0 \langle (\boldsymbol{v_1} \cdot \nabla) \boldsymbol{v_1} \rangle = -\nabla \cdot \langle p_2 \rangle + \mu \nabla^2 \langle \boldsymbol{v_2} \rangle + \left(\mu_b + \frac{\mu}{3} \right) \nabla (\nabla \cdot \langle \boldsymbol{v_2} \rangle) \qquad (3b)$$

where the angled bracket represents the time average of the quantity inside over an oscillation period. In Eq. (3), the products of the two first-order quantities lead to non-zero average values and act as the source terms that drive the second-order flow field. Physically, the non-zero averaged velocity $\langle \boldsymbol{v_2} \rangle$ corresponds to the acoustic streaming velocity. By assuming the fluid domain to be semi-infinite and neglecting the fluid viscosity, Shiokawa et al. [25] derived an analytical solution for the acoustic streaming force acting on the fluid induced by the leaky Rayleigh waves. However, we need to numerically solve Eq. (3) to obtain the streaming flow field to take into account the boundary effect, fluid viscosity, acoustic attenuation, *etc*.

2.3 Acoustophoretic forces on microparticles

In practical acoustophoretic applications, microchannels are often used to manipulate biological microparticles. These biological microparticles, such as cancer cells and white blood cells, are mainly made of water, so the gravity and buoyancy forces acting on them nearly cancel out. In our study, the densities of water and polystyrene particles are ρ_0 = 997 kg/m^3 and ρ_p= 1050 kg/m^3, respectively. The slight difference between ρ_0 and ρ_p leads to a non-zero resultant of the gravity and buoyancy forces. However, we assume that this net imbalanced vertical force is negligibly small as compared to the hydrodynamic forces. In other words, microparticles are assumed to be neutrally buoyant in the microchannel. Moreover, we assume that the particles in suspension are highly diluted and thus ignore particle-particle interactions. Therefore, the acoustophoretic motion of particles is determined by the acoustic radiation force ($\boldsymbol{F_{rad}}$) induced by acoustic scattering and the viscous drag force ($\boldsymbol{F_{drag}}$) arising from acoustic streaming.

Based on the solutions to the first-order equations, the time-averaged $\boldsymbol{F_{rad}}$ on a small spherical particle, whose size is much smaller than wavelength, can be calculated

as follows [26].

$$\boldsymbol{F_{rad}} = -\pi r^3 [\frac{2\kappa_0}{3} Re(f_1^* p_1^* \nabla p_1) - \rho_0 Re(f_2^* \boldsymbol{v_1^*} \cdot \nabla \boldsymbol{v_1})] \quad (4a)$$

where r is the particle radius, $\kappa_0 = \frac{1}{\rho_0 c_0^2}$ is the compressibility of the fluid, the asterisk represents complex conjugate, the function $Re()$ denotes the real part of the complex variable. The factors f_1 (real number) and f_2 (complex number) are:

$$f_1 = 1 - \frac{\kappa_p}{\kappa_0} \quad (4b)$$

$$f_2 = \frac{2(1-\tau)(\rho_p - \rho_0)}{2\rho_p + \rho_0(1-3\tau)} \quad (4c)$$

$$\tau = -\frac{3}{2}\left[1 + i\left(1 + \frac{\delta}{r}\right)\right]\frac{\delta}{r}, \quad \delta = \sqrt{\frac{2\mu}{\omega\rho_0}} \quad (4d)$$

where ρ_p and κ_p are the density and compressibility of the solid particle, respectively, δ is the viscous boundary layer thickness in oscillatory flows.

Once the solutions to the second-order equations are known, the time-averaged F_{drag} on a small spherical particle can be computed by [17]:

$$\boldsymbol{F_{drag}} = 6\pi\mu r\ (\langle \boldsymbol{v_2} \rangle - \boldsymbol{v_p}) \quad (5)$$

where $\boldsymbol{v_p}$ is the particle velocity and $\langle \boldsymbol{v_2} \rangle$ is the fluid streaming velocity.

Then, a Lagrangian description of the particle motion can be established according to the Newton's second law [27].

$$\frac{d(m_p \boldsymbol{v_p})}{dt} = \boldsymbol{F_{drag}} + \boldsymbol{F}_{rad} \quad (6)$$

where m_p is the particle mass.

3. Numerical model

3.1 Model setup

Fig. 1 gives a cross-sectional view of a typical SSAW-based device. The microchannel with PDMS walls is bonded onto the piezoelectrical substrate at the bottom. The piezoelectrical substrate is made of Lithium Niobite (LiNbO3) as mentioned in previous studies[9, 18, 28]. The channel is filled with water. A pair of metallic IDTs sit beside the channel on the surface of the piezoelectrical substrate. When harmonic electric signals are applied on IDTs, they will generate two SAWs propagating on the surface of the substrate in opposite directions. The interference of these two SAWs, whose amplitude and frequency are the same, forms the SSAW on the surface of the substrate [29]. From the fluid-substrate interface, the acoustic energy propagates into liquid inside the microchannel. The decay coefficient C_d is calculated based on the leaky SAW dispersion relationship detailed in Vanneste and Bühler [30]. For actuation frequencies of 6.65 MHz, 19.87 MHz, and 19.59 MHz in the three test cases below, the values of C_d are taken to be 116 m^{-1}, 367 m^{-1} and 364 m^{-1}, respectively.

As the SSAW is nearly uniform in the longitudinal direction of the microchannel, we can simplify the problem into a cross-sectional 2D model. In the longitudinal direction, *i.e.*, perpendicular to the page in Fig. 1, the movements of the liquid and microparticles can be regarded to be uniform. As seen in Fig. 2, the channel width is W in the x direction, and the channel height is H in the z direction. The impedance boundary conditions are used to model the PDMS walls, which is indicated as Bi in Fig. 2 [18]. The displacement function is used to model the effect of SSAW actuation at the interface between the piezoelectric substrate and the fluid, indicated as Bv in Fig. 2. In calculating particle trajectories, the no-slip boundary condition is employed at all four boundaries of the microchannel, which is consistent with previous studies [17, 18]. When a polystyrene microparticle hits the wall, its position is fixed, and its velocity is set to zero.

The boundary conditions for the three PDMS walls, marked as Bi in Fig. 2, are modelled with an impedance wall condition given as [18]:

$$n[-p_1 i + \eta(\nabla \cdot \boldsymbol{v_1} + (\nabla \cdot \boldsymbol{v_1})^T) - (\frac{2}{3}\mu - \mu_b)(\nabla \cdot \boldsymbol{v_1})i] = -Z_0(\boldsymbol{n} \cdot \boldsymbol{v_1}) \cdot \boldsymbol{n} \quad (7a)$$

$$Z_0 = \rho_{PDMS} \times c_{PDMS} \quad (7b)$$

where Z_0 is the acoustic impedance of the wall and $\boldsymbol{n}$ is an outward-pointing unit vector perpendicular to the solid surface. The density and sound speed of the PDMS (1:10) material, i.e., the ratio of the curing agent to the polymer base is 1:10, are used in specifying the impedance condition, as consistent with previous studies [17, 18, 31]. The PDMS wall is assumed to be thicker than the attenuation decay length, thus absorbs most of the transmitted acoustic energy with little reflection back into the fluid.

To calculate the velocity boundary condition at the bottom boundary Bv, the displacement functions are first obtained. For Rayleigh waves, the x and z components of the displacement have a phase difference of 90°, so points at the boundary undergo elliptical motion and the displacement functions can be given as [32, 33]:

$$u_x(x,t) = \gamma u_0 \left[e^{-C_d\left(\frac{W}{2}-x\right)} e^{i\left[-k\left(\frac{W}{2}-x\right)+\omega t\right]} + e^{-\left(\frac{W}{2}+x\right)} e^{i\left[-k\left(\frac{W}{2}+x\right)+\omega t\right]} \right] \quad (8a)$$

$$u_z(x,t) = -u_0 \left[e^{-C_d\left(\frac{W}{2}-x\right)} e^{i\left[-k\left(\frac{W}{2}-x\right)+\omega t-\frac{\pi}{2}\right]} - e^{-\left(\frac{W}{2}+x\right)} e^{i\left[k\left(\frac{W}{2}+x\right)+\omega t-\frac{\pi}{2}\right]} \right] \quad (8b)$$

where u_0 is the maximum amplitude of the z-component SAW displacement equal to 0.1 nm in the present study, $k = 2\pi/\lambda$ is the wavenumber, γ is the ratio between the x-component and the z-component. By differentiating Eq. (8) with respect to time, the first-order velocity imposed over Bv can be obtained. In the frequency domain analysis, the time-dependent terms are removed. Therefore, the velocity boundary condition can be given as:

$$v_x(x,t) = \gamma u_0 \omega \left[e^{-C_d\left(\frac{W}{2}-x\right)} e^{i\left[-k\left(\frac{W}{2}-x\right)\right]} + e^{-\left(\frac{W}{2}+x\right)} e^{i\left[-k\left(\frac{W}{2}+x\right)\right]} \right] \quad (9a)$$

$$v_z(x,t) = -u_0 \omega \left[e^{-C_d\left(\frac{W}{2}-x\right)} e^{i\left[-k\left(\frac{W}{2}-x\right)-\frac{\pi}{2}\right]} - e^{-\left(\frac{W}{2}+x\right)} e^{i\left[k\left(\frac{W}{2}+x\right)-\frac{\pi}{2}\right]} \right] \quad (9b)$$

In the present study, the temperature is taken to be T=25℃, which is the same as that in previous studies [17, 18]. At this temperature, the key properties of water are $\rho_0 = 997$ kg/m^3, speed of sound $c_0 = 1497$ m/s, $\mu = 0.890$ mPa s, $\mu_b = 2.47$ mPa s, and $\kappa_0 = 448$ T/Pa; the values of the key parameters of polystyrene are $\rho_p = 1050$ kg/m^3, $c_p = 2350$ m/s, and $\kappa_p = 249$ T/Pa; the key properties of PDMS (10: 1) are $\rho_{PDMS} = 920$ kg/m^3, and speed of sound $c_{PDMS} = 1076.5$ m/s [31, 34-38].

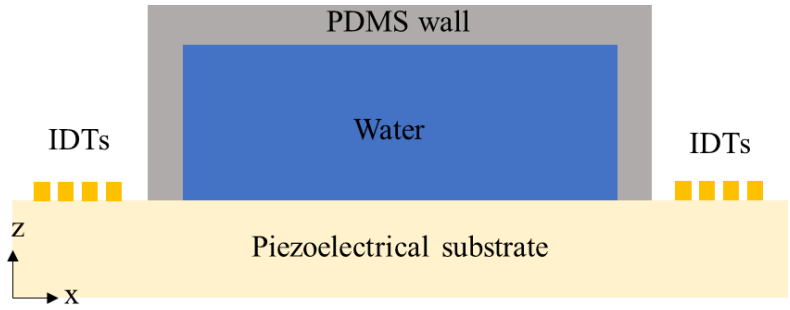

Fig. 1 Cross-sectional view of a SSAW-based microfluidic device

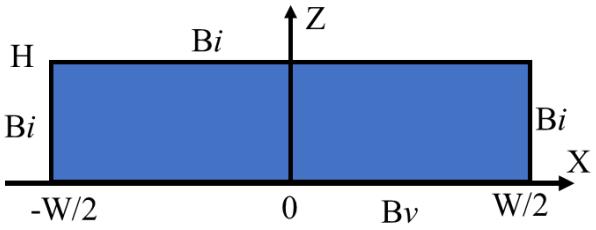

Fig. 2 Sketch of the computational domain

3.2 Numerical procedure

The FEM simulation is implemented as follows. First, the Thermoacoustic Physics Interface Module is used to calculate the first-order acoustic field by solving the linearised compressional Navier-Stokes equation and the continuity equation, Eq. (2), in the frequency domain. In this step, the acoustic pressure p_1 and acoustic velocity $\boldsymbol{v}_1$ are determined. Secondly, the Laminar Flow Physics interface is used to calculate

the time-averaged second-order flow field using Eq. (3), with the known first-order quantities. The streaming pressure p_2 and streaming velocity v_2 are obtained. Thirdly, the acoustic radiation forces and drag forces are determined using Eq. (4) and Eq. (5), respectively, using the results obtained in step 1 and step 2. Finally, combining the acoustic radiation forces and drag forces, the velocity and displacement of the microparticles are computed based on Eq. (6) in the Particle Tracing Module. The predicted acoustophoretic particle trajectories can be compared with those observed in microfluidic experiments.

3.3 Mesh Convergence Analysis

The computational mesh is generated by allocating small elements near the boundary and large element in the bulk of the domain, so as to resolve the small flow structures in the wall boundary layers [17]. The minimum element length is denoted by d_b, while the maximum element is around 10 times larger. In the mesh convergence study, the element size d_b is gradually decreased. The relative convergence function *C(g)* is defined by Eq. (10):

$$C(g) = \sqrt{\frac{\int (g - g_{ref})^2 dxdz}{\int (g_{ref})^2 dxdz}} \tag{10}$$

where g represents the computed p_1 $\boldsymbol{v_1}$ or $< \boldsymbol{v_2} >$, while g_{ref} represents the solution corresponding to the finest mesh with 5.6×10^5 elements and $d_b = 0.2\delta$ [18]. The finest mesh is illustrated in Fig. 3(a).

The semi-logarithmic plot in Fig. 3(b) shows the decrease of the convergence function with the increase of the mesh resolution in a typical simulation. The mesh resolution is quantified by δ/d_b, which is the ratio of the boundary layer thickness estimated by Eq. (4d) to the minimum element size. In order for relative convergence function to fall below 0.002 for all of the computed variables, a mesh with $d_b < 0.3\delta$ is required. In all of the subsequent simulations, this criterium has been satisfied.

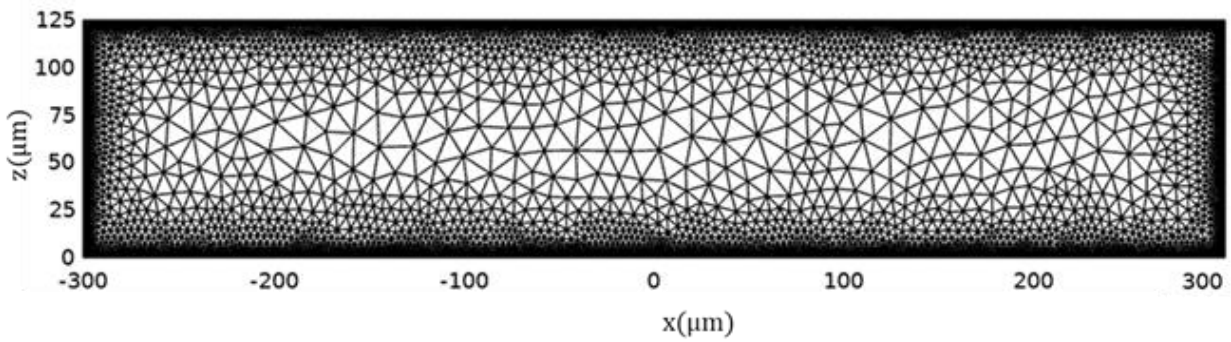

(a) Computational mesh with $d_b = 0.2\delta$

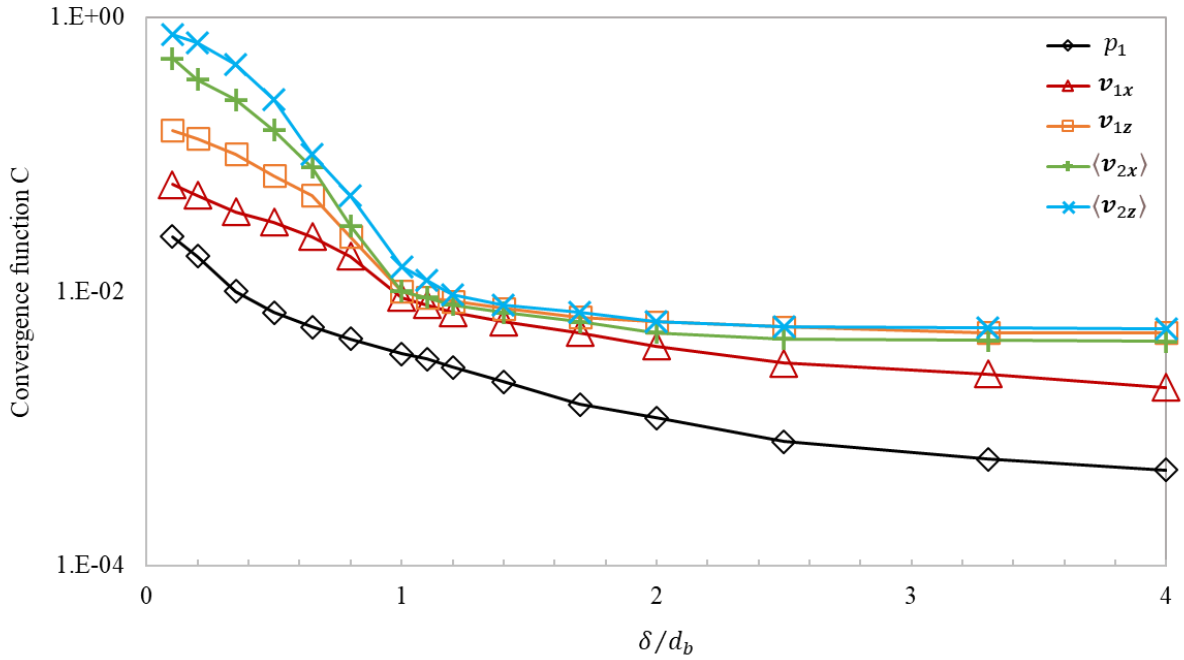

(b) Relative convergence parameter C as a function of the mesh resolution

Fig. 3 Mesh convergence analysis

4. Model verifications

4.1 Verification against Nama et al.[18]

In the case study of Nama et al. [18], the LiNbO3 piezoelectric substrate is actuated with a surface wave of wavelength λ = 600 μm and frequency f = 6.65 MHz. The width of the microchannel is equal to the wavelength, while the height of the channel is 125 μm.

Fig. 4 shows the distribution of the first-order pressure field p_1, the first-order velocity field $\boldsymbol{v_1}$, the second-order velocity field $\langle \boldsymbol{v_2} \rangle$ and particle trajectories obtained with the numerical model established in Section 3. The simulation results agree well with those presented in Nama et al. [18], which verify the correctness of the model and the good resolution of the computational mesh. In Fig. 4(a), a horizontal standing wave pattern is clearly visible along the channel width. The introduced acoustic waves at the bottom boundary propagate upwards, as indicated by the two blue arrows. The maximum amplitude of the first-order pressure oscillation is 12.9 kPa. Fig. 4(b) reveals that the maximum amplitude of the first-order velocity occurs at the mid-height level and is 5.4 mm/s. Fig. 4(c) shows that the maximum second-order velocity $\langle \boldsymbol{v_2} \rangle$ is equal to 1.47 $\mu m/s$, which happens in the boundary layer of the bottom wall. Four streaming vortices can be observed, which span the height of the channel.

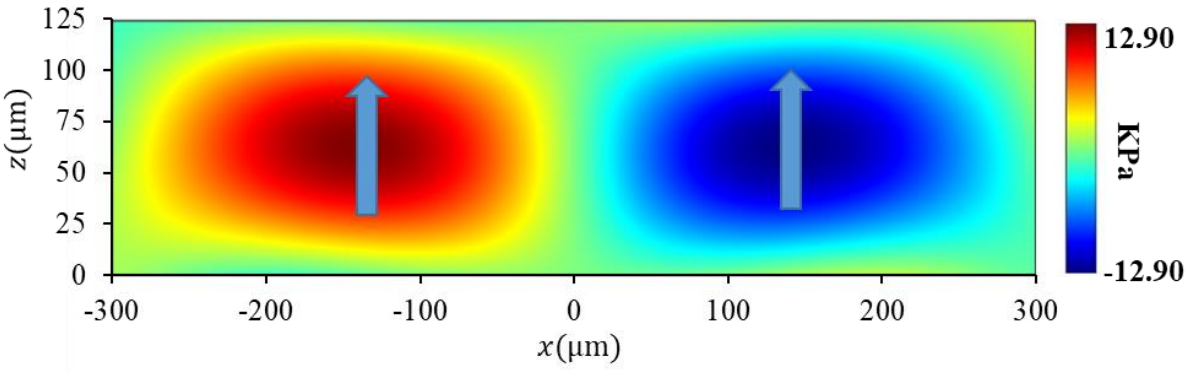

(a) First-order pressure field p_1

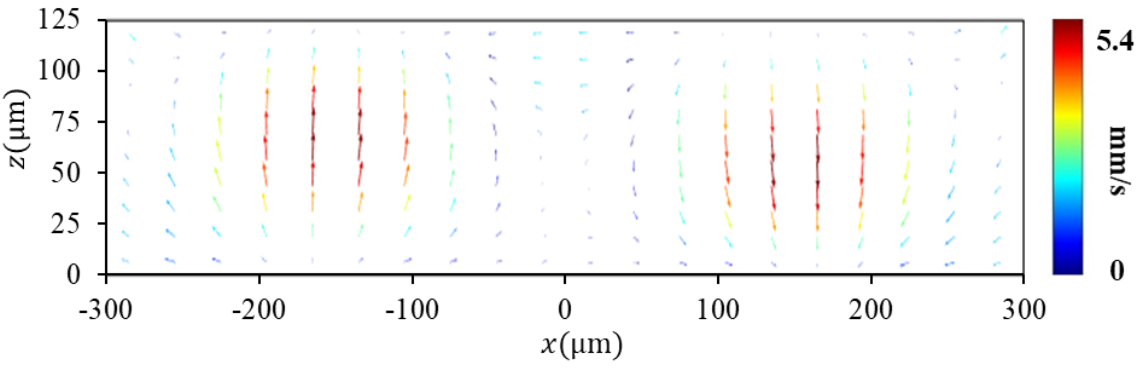

(b) First-order velocity field $\boldsymbol{v_1}$

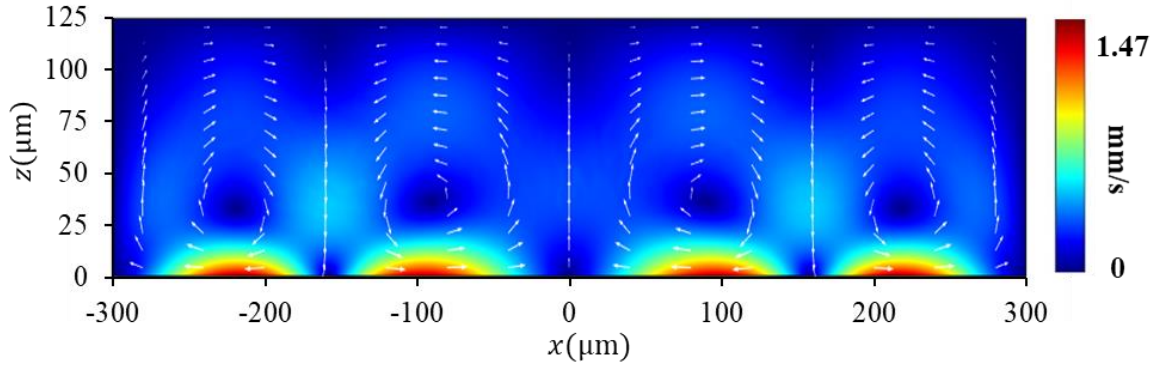

(c) Time-averaged second-order velocity field $\langle \boldsymbol{v_2} \rangle$

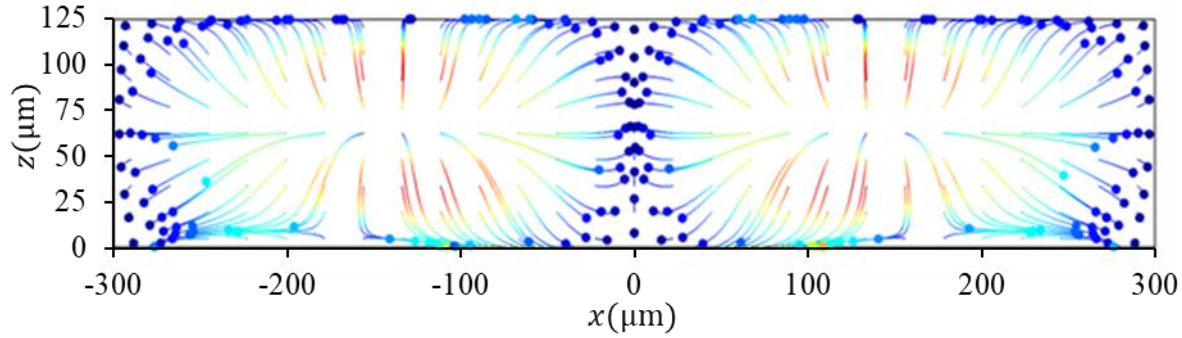

(d) Trajectories of the 243 particles in 40 seconds

Fig. 4 Verification against the setup in Nama et al. [18]

In calculating the velocities and displacements of the polystyrene particles, 243 particles each with a radius of $10\ \mu m$ are uniformly distributed in the channel at t = 0 s, forming a 27×9 matrix. Subjected to the acoustic radiation force, these particles move to the channel centre and two sides. The Stokes drag force is much smaller than the acoustic radiation force in this case. Fig. 4(d) demonstrates a snapshot of the particle positions at t = 40 s, indicated by circular dots, and the trajectories of the particle, indicated by coloured lines. The colour of a line changes to reflect the instantaneous velocity of the particle as it moves. The blue and red colours represent zero and the maximum velocity of $4.1\ \mu m/s$, respectively. It can be seen that almost all the circular dots in Fig. 4(d) are blue, implying that particles move slowly at the moment t = 40 s. The results shown in Fig. 4(d) agree well with those presented in Nama et al.[18].

4.2 Verification against Mikhaylov et al. [22]

Mikhaylov et al. [22] developed a novel technology to use the printed circuit board (PCB) with a piezoelectric substrate to improve the fabrication of SAW devices. The acoustic wavelength is $\lambda = 200$ μm, and frequency is $f = 19.87$ MHz. In the experiment, the two IDTs are made of arrays of metallic electrodes, and the input power is 0.5 W. The channel height is 60 μm. Initially, 15×5 polystyrene particles each with a radius of 5 μm are evenly distributed in the channel.

Fig. 5(a) presents the acoustic pressure field when the PN is located at the centre of the microchannel. In Fig.5(d), the phase of the AC signal is shifted by 180°, making the AN to be located at the centreline of the microchannel. The particle displacements are tracked until particles have reached their final positions. Figs. 5(b) and (e) demonstrate the particle trajectories when the PN and AN are located at the channel centreline, respectively. It takes 13 s and 7 s for particles to reach final positions in the two cases shown in Figs 5(b) and (e), respectively. Three microparticle aggregation traces are predicted in Fig. 5(b), and five are predicted in Fig. 5(e), which generally match the experiment results as shown in Fig. 5(c) and 5(f), respectively. However, in the second case, the particle aggregation at the AN along the channel centreline is unstable and is sensitive to any force imbalance, hence the yellow dot as shown in Fig. 5(e). Therefore, particles tend to shift to the adjacent stable PN locations instead, which is why only four microparticle aggregation traces can be observed in Fig. 5(f).

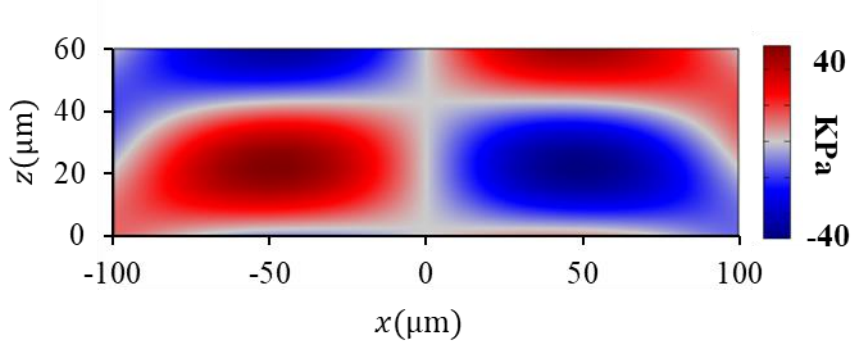

(a) Acoustic pressure field with PN located at the channel centreline

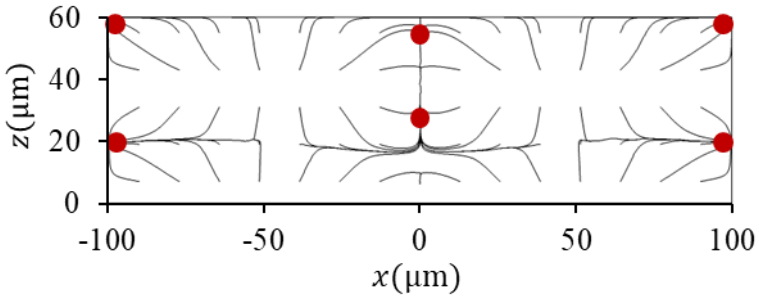

(b) Particle trajectories with PN located at the channel centreline

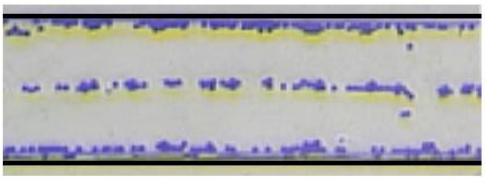

(c) Microscopic image showing three cell traces when a SSAW PN is located at the channel centreline

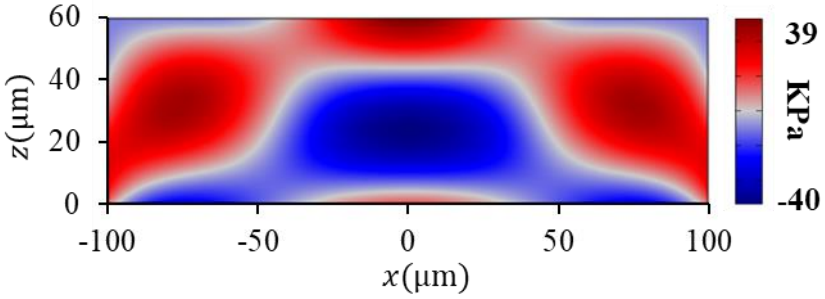

(d) Acoustic pressure field with AN located at the channel centreline

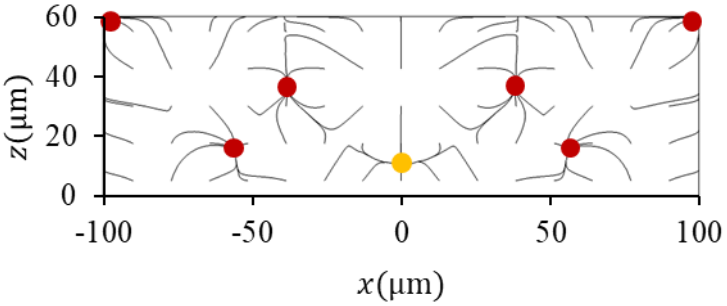

(e) Particle trajectories with AN located at the channel centreline

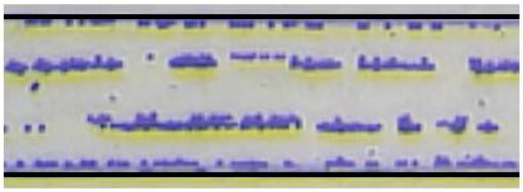

(f) Microscopic image of four cell traces when applying a SSAW AN is located at the channel

centreline

Fig. 5 Verification against the setup in Mikhaylov et al. [22]

4.3 Verification against Sun et al. [16]

Sun et al.[16] used Gallium Nitride (GaN) as the piezoelectric substrate instead of Lithium Niobate to overcome the high cost and brittleness of the bulk Lithium Niobate material. A surface wave is applied with wavelength λ = 280 μm and frequency f = 19.59 MHz. The two-dimensional electron gases are used as IDTs, and each contains 40 pairs of finger electrodes with an aperture size of 7 mm. The input power is 1.9 W. The height of channel is 60 μm. Initially, 25×8 polystyrene particles each with a radius of 5 μm are evenly distributed in the channel.

Fig. 6(a) shows the amplitude of the acoustic pressure field, with the pressure node (PN) located at the centre of the microchannel. The range of the pressure amplitude is from 0 to 60 kPa. Then, a pressure AN is set at the centreline of the microchannel after the phase of the AC signal is shifted by 180° and Fig. 6(d) demonstrates the amplitude of acoustic pressure. The range of the pressure amplitude is from 0 to 84 kPa. Fig. 6(b) illustrates the particle trajectories at t = 25 s when the PN is located at the centreline of the microchannel, which leads to three aggregation traces in the plan view as experimentally observed in Fig. 6(c). Fig. 6(e) shows the particle trajectories at t =10s when the AN is located at the centre of the microchannel, with five microparticle aggregation traces in the plan view as experimentally observed in Fig. 6(f).

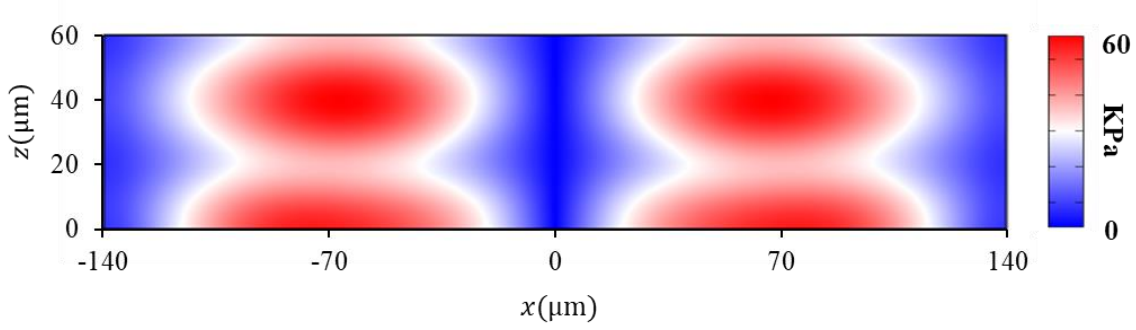

(a) Acoustic pressure field with PN located at the channel centreline

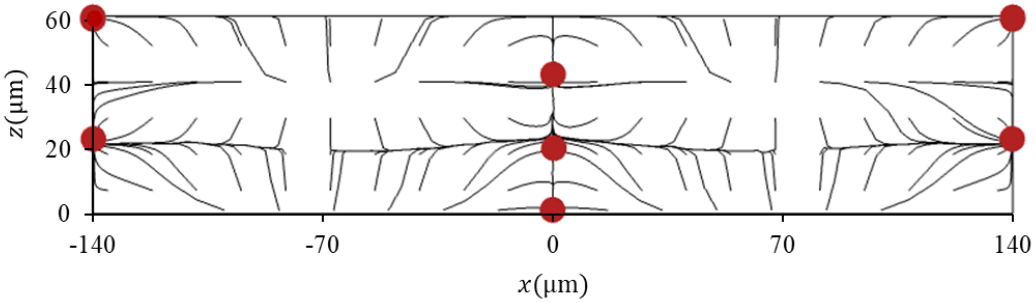

(b) Particle trajectories with PN located at the channel centreline (t=25s)

(c) Experimental result showing particle aggregation with PN located along the channel centreline

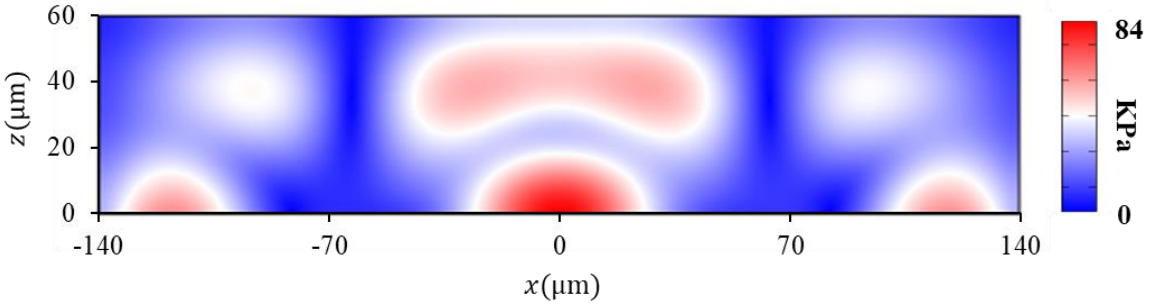

(d) Acoustic pressure field with AN located at the channel centre

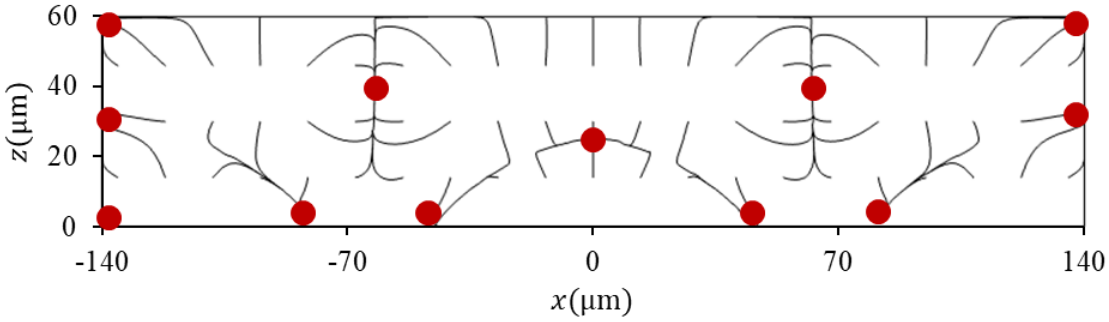

(e) Particle trajectories with AN located at the channel centreline (t=10s)

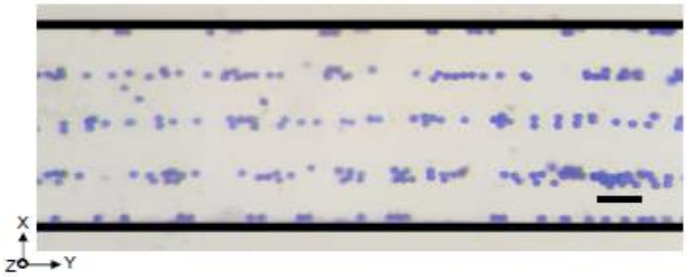

(f) Experimental result showing particle aggregation with AN located along the channel centreline

Fig. 6 Verification against the setup in Sun et al. [16]

5. Parametric studies

5.1 Influence of particle size

This section uses the validated model to study the sensitivity of results to the particle size, while the wavelength and frequency of the actuating SSAW are fixed at 600 μm and 6.65 MHz, respectively. Based on the theory given in Section 2, the viscous drag force is proportional to the particle radius, while the acoustic radiation force is proportional to the particle volume. Hence, we expect that the viscous drag force becomes dominant for small particles while the acoustic radiation force becomes dominant for large particles. A total of 22 sizes of polystyrene particles are examined, with the radius ranging from 0.1 μm to 15 μm. The simulation time is 100 s – long enough to reveal the trend of the particles' motion. Fig. 7 only show the results of 3 representative particle sizes to demonstrate the key findings. The colours of the particle trajectories indicate the particle velocities ranging from zero (blue) to maximum (red). The solid circle of each trajectory indicates the final position of a particle at t =100 s. Fig. 7(a) shows that particles circulate inside four streaming vortices with a maximum velocity of around 1.48 μm/s, which is almost equal to the maximum streaming velocity. The movement of small particles with a radius of 0.5 μm is entirely dominated by the viscous drag force. As the particle size increases, the acoustic radiation force

becomes more influential. As can be seen from Fig. 7(b), the pattern of the streaming eddies vanishes in particle trajectories with a radius of 4 μm. The acoustic radiation force plays an important in the movement of these larger particles, driving them to the PNs in the middle and at the two sidewalls. As the particles size keeps increasing, the movement of the particles is totally determined by the acoustic radiation force and particle aggregation is achieved, as seen in Fig. 7(c).

To further evaluate the influence of the particle size on the acoustophoretic motion, the ratio of the maximum magnitude between the acoustic radiation force and the viscous drag force, $|\boldsymbol{F_{rad}}|/|\boldsymbol{F_{drag}}|$, is plotted in Fig. 8 as a function of the particle size. Although the ratio of these two forces is position-dependent, we hereby choose the maximum values of the forces over the entire cross-section to compare their relative magnitude. When the particle radius is less than 4 μm, this ratio is less than 1.0, implying that the particles' motion is mainly determined by the viscous drag force. When the radius is 4-6 μm, $|\boldsymbol{F_{rad}}|/|\boldsymbol{F_{drag}}|$ is close to 1, implying the transition from the streaming-dominated motion to the radiation-dominated motion. As the particle size increases further, this ratio continuously increases to be much greater than 1.0. When the radius is 6-8 μm, particles are mainly governed by the acoustic radiation force. The influence of the drag force can be neglected when the radius exceeds 8 μm.

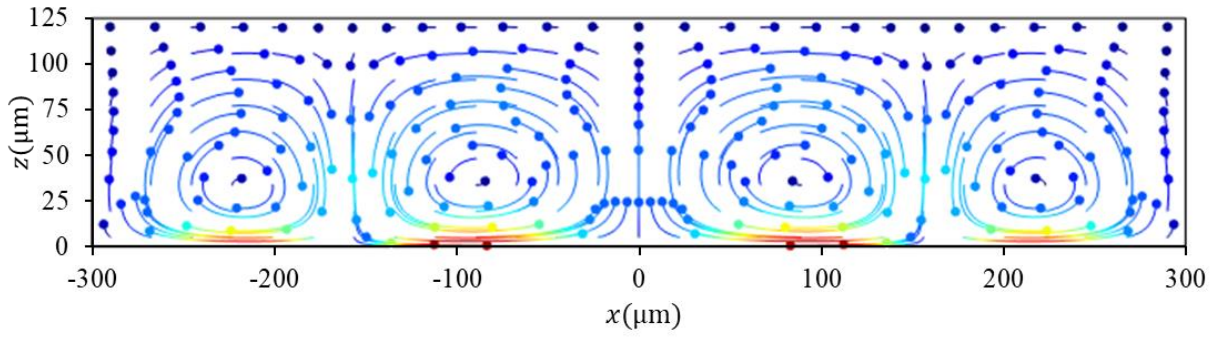

(a) r=0.5 μm, $u^{max} = 1.48$ μm/s

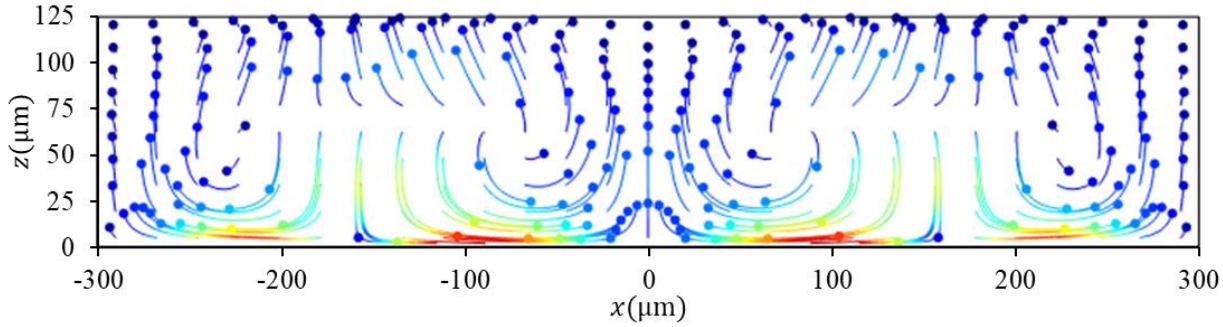

(b) r=4.0 μm, $u^{max} = 1.95$ μm/s

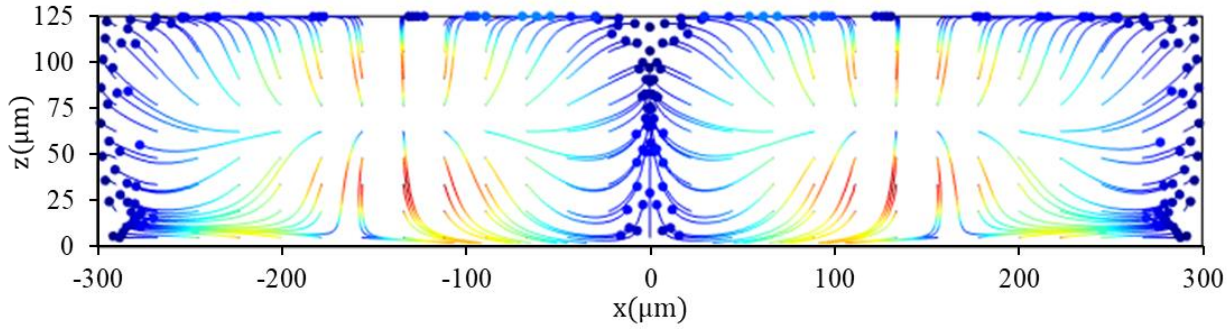

(c) r=8.0 μm, $u^{max} = 3.34$μm/s

Fig. 7 Trajectories of particles of different radii

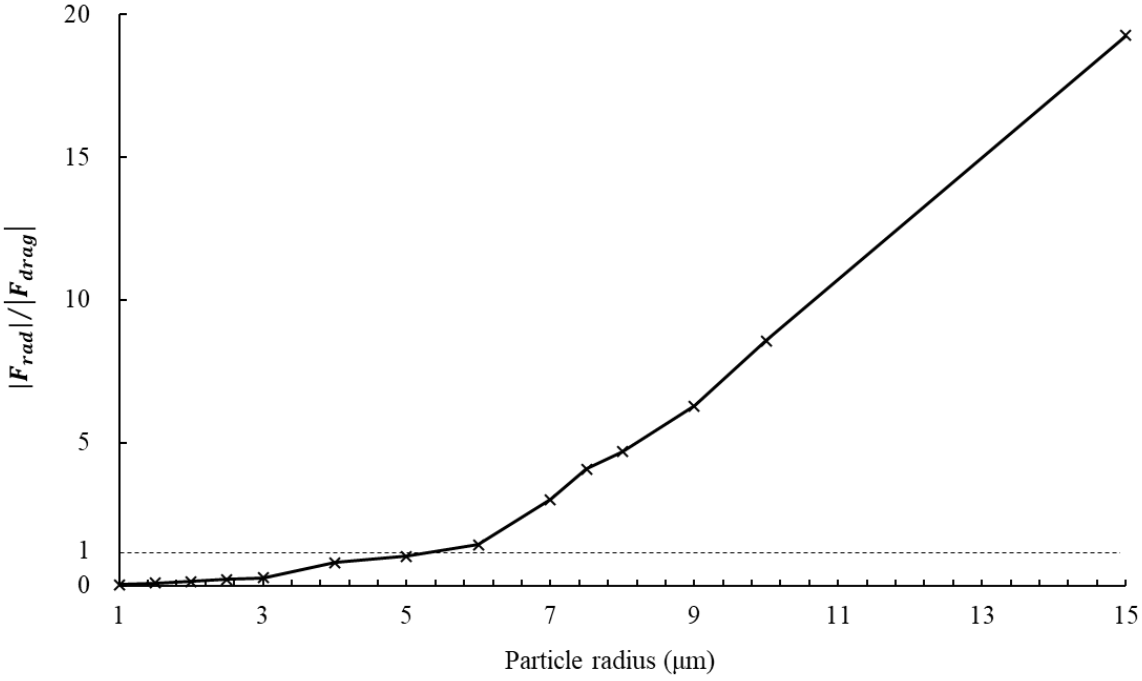

Fig. 8 Ratios of the maximum acoustic radiation force to the maximum viscous drag force at

different particle sizes

5.2 Influences of channel height

There has not been any research on the influence of the microchannel height on the particle acoustophoresis, hence the topic of this section. In Fig. 9, the configurations are exactly the same as those in Nama et al.[18], except the channel height. As shown in Fig. 9(a), some particles are stuck to the bottom and top walls, rather than move to the PN and AN, when the channel height is small. Such a phenomenon may be attributed to the large vertical component of the resultant force on these particles as compared to the horizontal component. With such a microchannel height, the efficiency of particles aggregation is low. By changing the height of the channel, the directions of resultant forces on the near-boundary particles varies. In order to obtain a convincing conclusion, extensive parametric studies are conducted based on all three verified cases in Section 4.

In the parametric study, the channel height ranges from 100 μm to 225 μm, the particle radius is 10 μm, the physical time of simulation is 100 s and the input SAW displacement amplitude (u_0) of $0.1\,\mathrm{nm}$. It should be noted that the displacement amplitude of the imposed SAW only affects the time scale of the particle movement but does not affect the destination of the particles. In our study, we focus on the final positions of particles. Hence, the following findings are also valid for other SAW amplitude. A total of 20 heights have been simulated, but only 6 are illustrated in Fig. 9 to highlight the influences of the channel height. As the height of channel increases, fewer particles are stuck to the bottom and top walls. When the height is equal to 129 μm, almost all the particles can move to PNs. Such a good performance is kept until the height exceeds 184 μm. Some particles start to stay on the bottom wall again when the height gradually increased from 185 μm to 225 μm. Therefore, in order to be able to sort out particles, the channel height should lie in certain ranges.

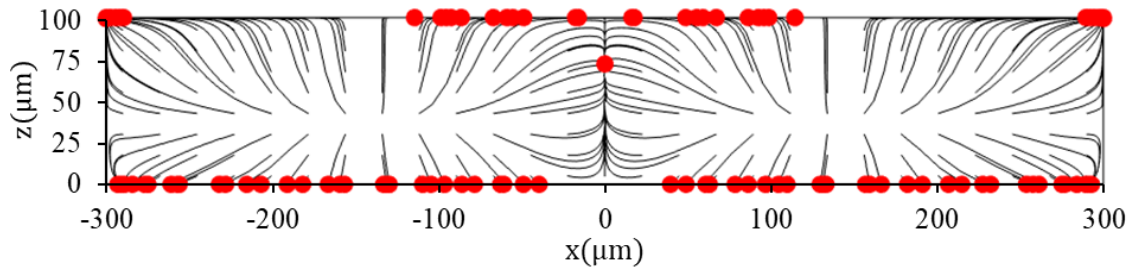

(a) H=100 μm

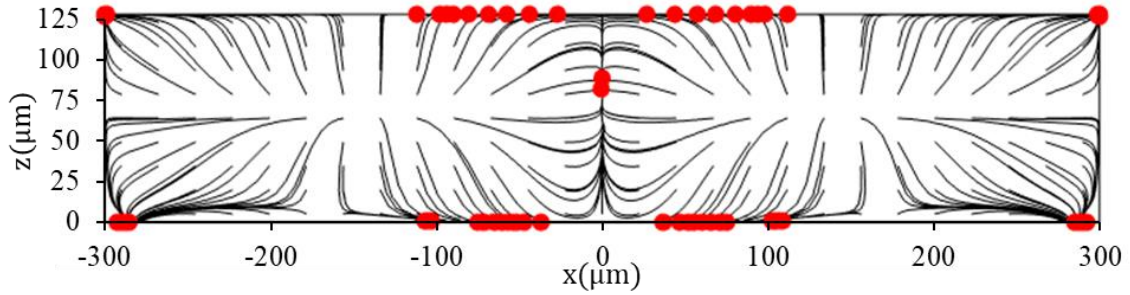

(b) H=125 μm

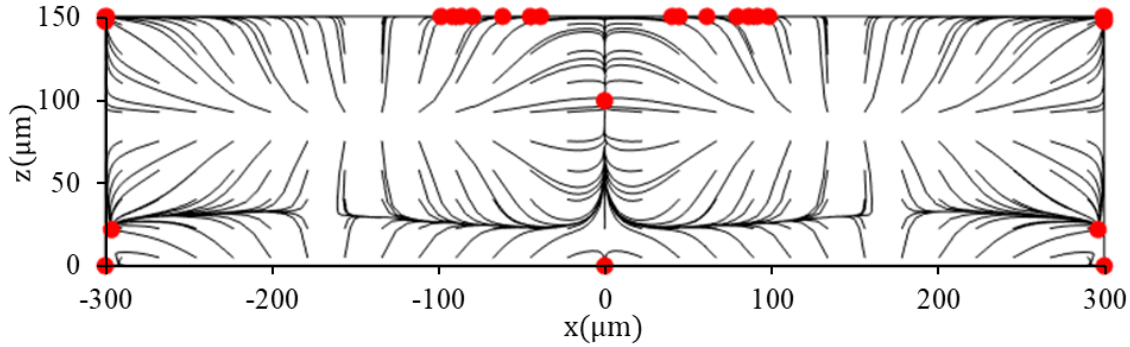

(c) H=150 μm

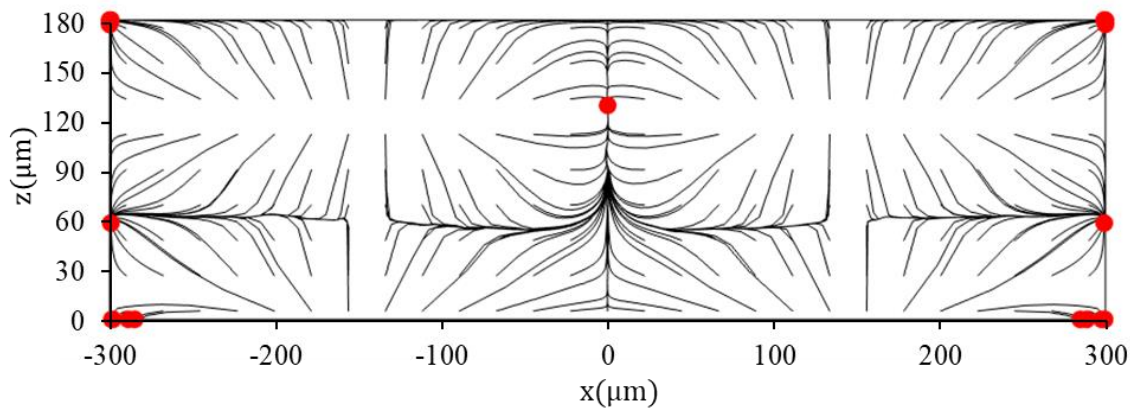

(d) H=180 μm

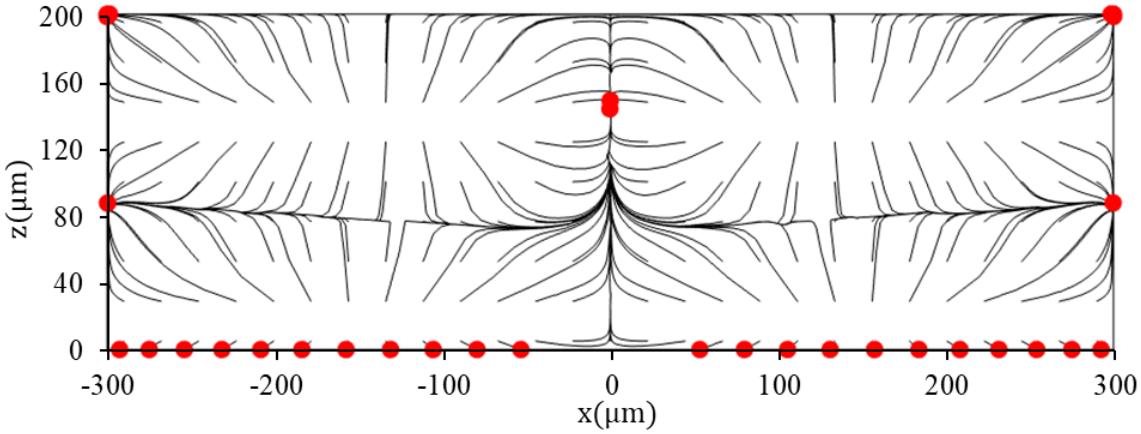

(e) H=200 μm

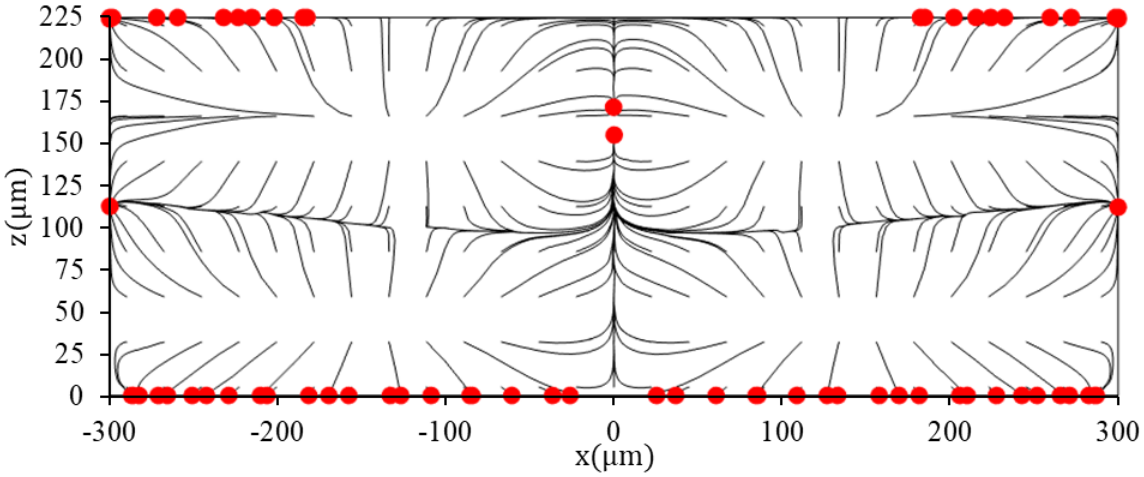

(f) H=225 μm

Fig. 9 Influence of the channel height on particle positions

In order to quantify the particle distribution, we plot the particle histogram along the channel width. The number of particles is counted in every 40 μm intervals along the *x* axis. The optimum heights are defined as the heights that allow more than 95% of particles to accumulate at PNs. Fig. 10 demonstrates the example particle histograms corresponding to the heights less than, more than and exactly within the range of the optimum height. Fig. 10(b) shows that H = 180 μm is within the range of optimum height and the aggregation efficiency is 100%; Figs. 10 (a, c) demonstrate that H = 100 μm and H = 225 μm are outside the range of optimum height and the aggregation efficiency is less than 95%, i.e., 66% and 83% respectively. Fig. 11 shows how the

percentage of particles arriving at the aggregation points varies with the channel height, which indicates the optimum height range is from 129 μm to 185 μm.

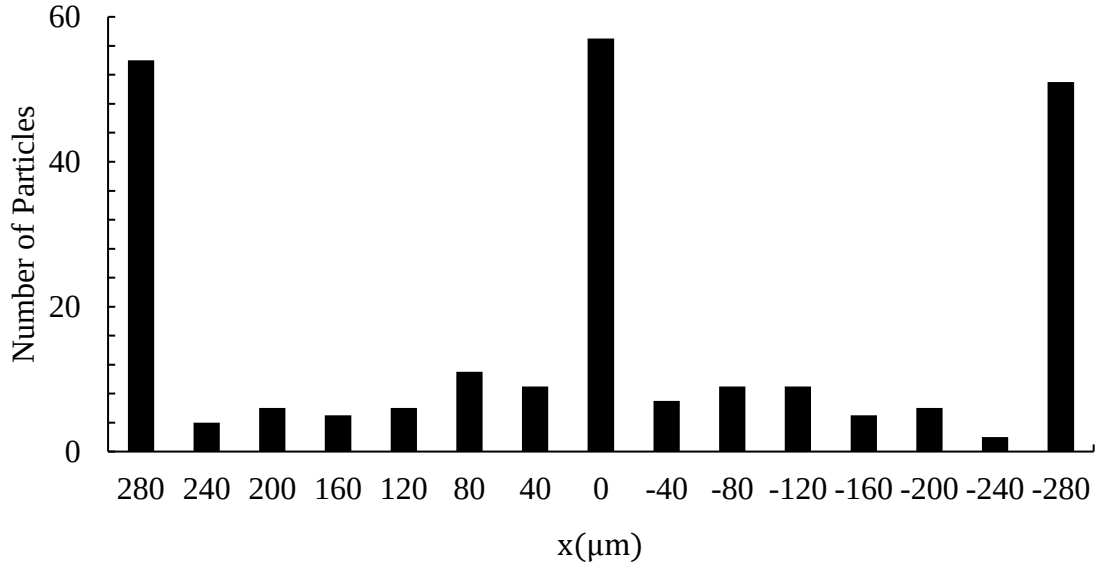

(a) H=100 μm

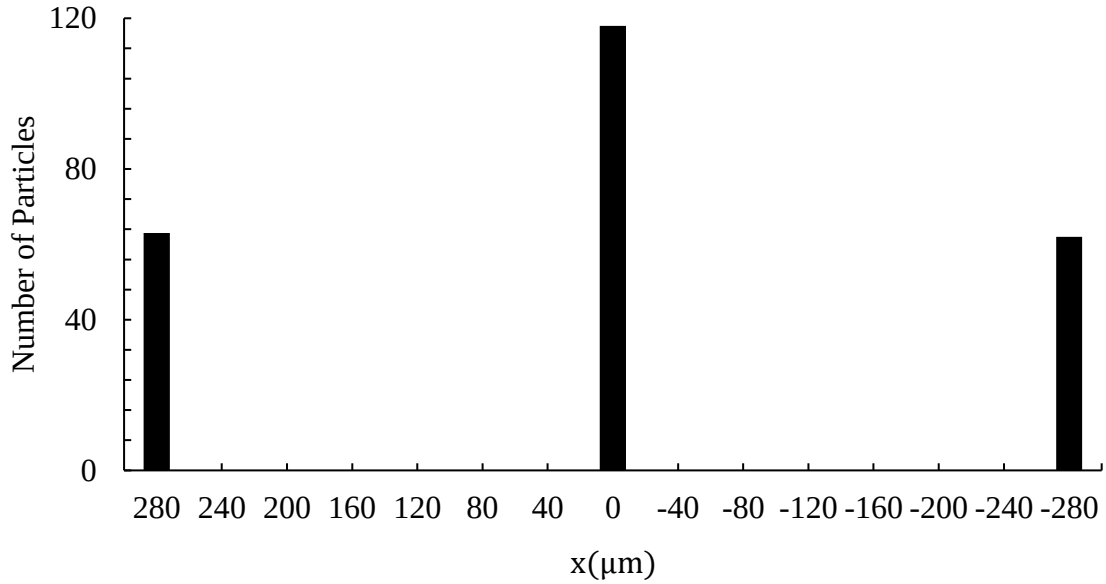

(b) H=180 μm

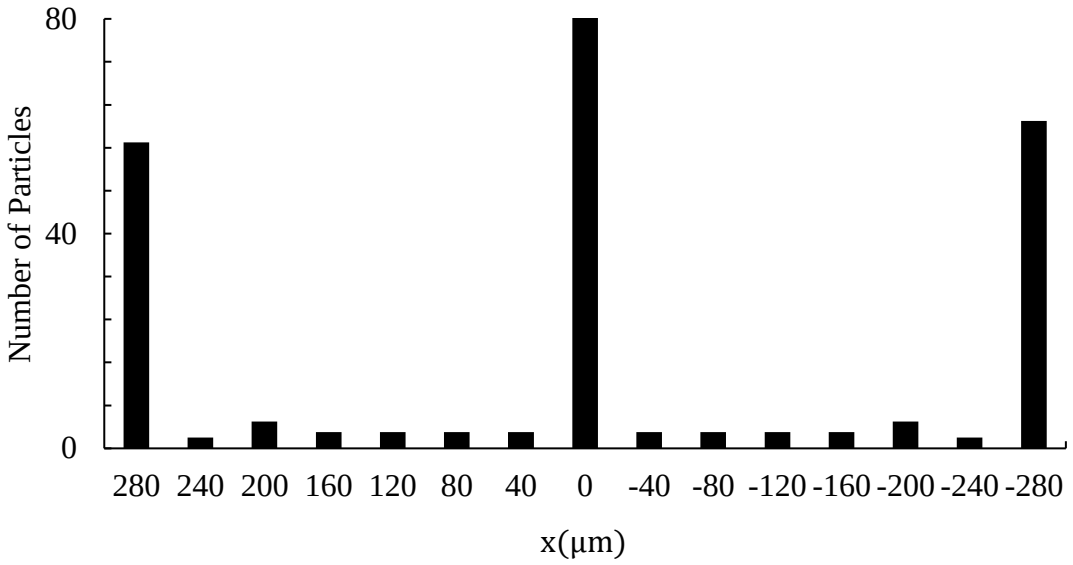

(c) H=225 μm

Fig. 10 Particle distribution at different channel heights

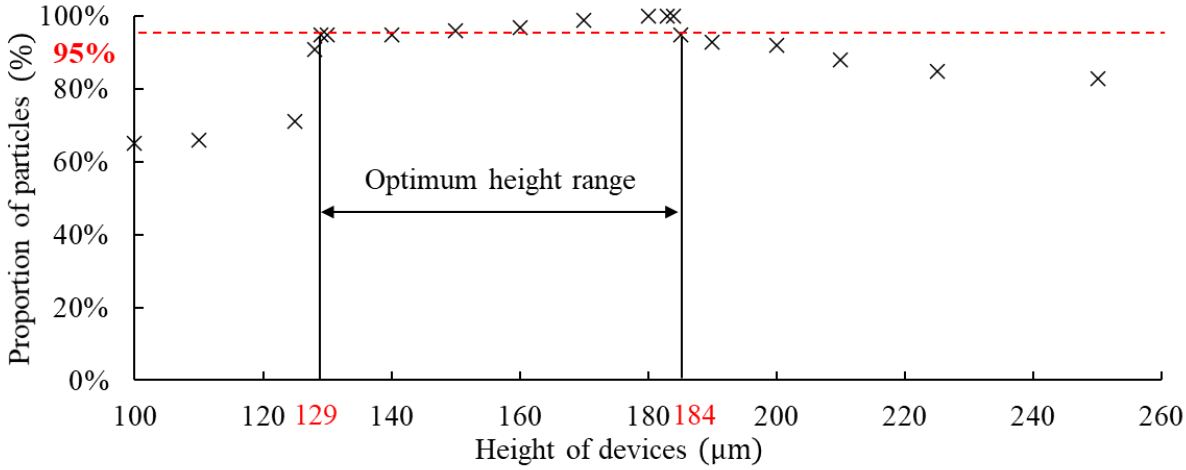

Fig. 11 Proportions of the aggregated particles at different channel heights in the setup of Nama et al. [18]

It can be noticed that the acoustic wave propagates periodically in the vertical direction, with the wavelength:

$$\lambda_f = c_0/f \tag{11}$$

where λ_f is the wavelength in the fluid, which can be calculated to be 225 μm from the speed of sound of the fluid $c_0 = 1497$ m/s and the frequency of the acoustic wave $f = 6.65$ MHz.

By normalising the channel height with the acoustic wavelength in the fluid, the dimensionless optimum height can be obtained. In this case, H_{min} and H_{max} are 129 μm 184 μm, respectively. Therefore, we have H_{min}/λ_f=0.57 and H_{max}/λ_f=0.82 for the setup in Nama et al. [18]

The same process can be repeated for the other two setups as included in the model verification. Fig. 12 and Fig. 13 show how the percentage of particles reaching the PNs for these two setups. The ranges of dimensionless optimum height are summarised in Table 1. From Table 1, it can be concluded that the dimensionless optimum heights in three models are consistent and the average range is from 0.57 to 0.82. These values are independent of the channel dimensions and acoustic wave inputs.

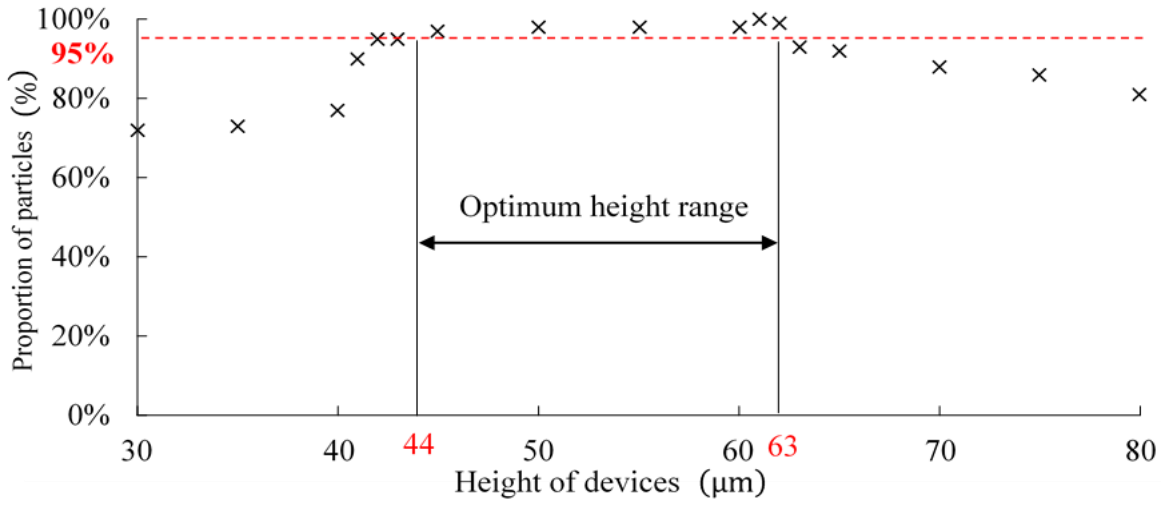

Fig. 12 Proportions of the aggregated particles at different channel heights in the setup of Sun et al. [16]

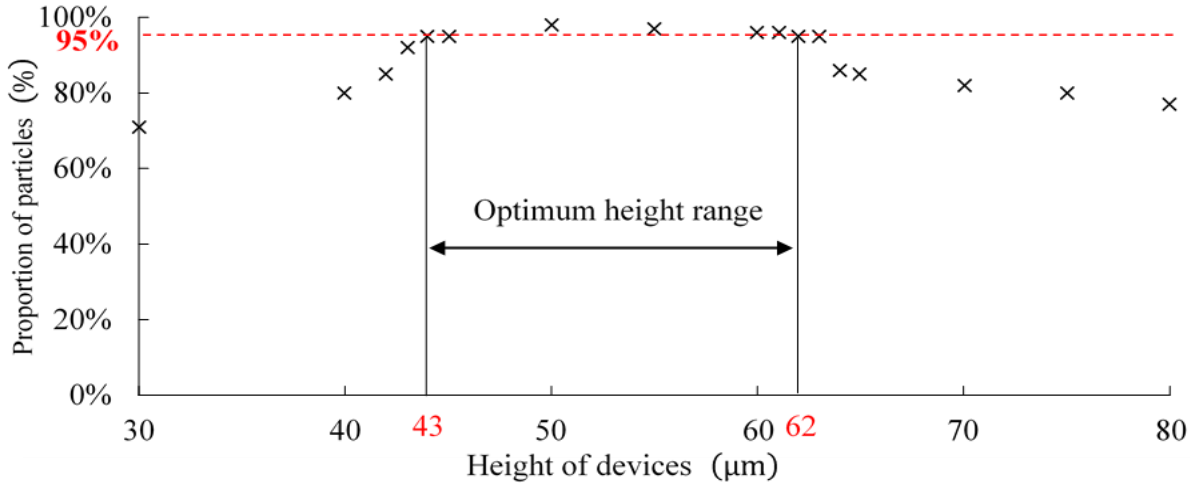

Fig. 13 Proportion of the aggregated particles at different channel heights in the setup of Mikhaylov et al. [22]

Table 1 Range of the dimensionless optimum height of the channel

Setup	Speed of sound in fluid (m/s)	Frequency (MHz)	Vertical wavelength (μm)	Optimal height (μm)	Dimensionless optimum height
Nama et al.[18]	1497	6.65	225	129-184	0.57-0.82
Sun et al.[16]	1497	19.4	77.1	44-63	0.57-0.81
Mikhaylov et al.[22]	1497	19.88	75.3	43-62	0.57-0.82
Average	-	-	-	-	0.57-0.82

6. Conclusions

A perturbation-based FEM model has been established to study the acoustophoretic motion of microparticles. The motion of particles is governed by the acoustic radiation force, induced by scattering of sound waves, as well as the viscous drag force, induced by acoustic streaming. These two forces are related to the first-order and second-order flow solutions, respectively. The model has been verified against

three past cases reported in the literature.

The numerical model is then used to study the influence of the particle size. In our study, the microchannel walls are made of PDMS (10:1), the liquid inside the channel is water and the microparticles are polystyrene spheres. With the bottom actuation wavelength and frequency of 600 μm and 6.65 MHz, respectively, the trajectories of polystyrene particles with radius from 0.1 μm to 15 μm are calculated. The motion of particles smaller than 4 μm is dominated by the viscous drag force, while the particles between 4-6 μm exhibit transition pattern from the streaming-dominated motion to the acoustic-dominated motion. Particles between 6-8 μm are governed by the acoustic radiation force, while the influence of the drag force can virtually be neglected once the radius exceeds 8 μm. Under the considered material and actuation condition, the threshold radius is found to be 4-6 μm. Only the particles larger than this size can effectively aggregate towards the PNs of the acoustic field and thus sorted out from the ambient liquid.

With the width of the micro-channel fixed to one wavelength, the optimum height of the channel is investigated in the second application. The direction of the resultant force acting on the particles depends on the height of the devices. Different heights lead to different proportions of the particles that accumulate at PNs. To achieve a good aggregation efficiency, the optimum height, corresponding to the accumulation of more than 95% particles, has been found to be between 0.57 and 0.82 times the acoustic wavelength in the fluid.

7. Acknowledgements

The work has been supported by the Cambridge Tier-2 system operated by the University of Cambridge Research Computing Service (http://www.hpc.cam.ac.uk) funded by EPSRC Tier-2 capital grant EP/P020259/1.

8. References

[1] P. Mitchell, Microfluidics—downsizing large-scale biology, Nature biotechnology 19, 8 (2001) 717–721.
[2] D.J. Beebe, G.A. Mensing, G.M. Walker, Physics and Applications of Microfluidics in Biology, Annual Review of Biomedical Engineering, 4 (1) (2002) 261-286.
[3] E.K. Sackmann, A.L. Fulton, D.J. Beebe, The present and future role of microfluidics in biomedical research, Nature, 507 (2014) 181-189.
[4] J.Y. Hwang, C.W. Yoon, H.G. Lim, J.M. Park, S. Yoon, J. Lee, K.K. Shung, Acoustic tweezers for studying intracellular calcium signaling in SKBR-3 human breast cancer cells, Ultrasonics, 63 (2015) 94-101.
[5] H. Li, J. Friend, L. Yeo, A. Dasvarma, K. Traianedes, Effect of surface acoustic waves on the viability, proliferation and differentiation of primary osteoblast-like cells, Biomicrofluidics, 3 (2009) 034102.
[6] F. Petersson, L. Åberg, A.-M. Swärd-Nilsson, T. Laurell, Free flow acoustophoresis: microfluidic-based mode of particle and cell separation, Analytical chemistry, 79 (2007) 5117-5123.
[7] M. Wiklund, Acoustofluidics 12: Biocompatibility and cell viability in microfluidic acoustic resonators, Lab on a Chip, 12 (2012) 2018-2028.
[8] X. Ding, S.-C.S. Lin, B. Kiraly, H. Yue, S. Li, I.-K. Chiang, J. Shi, S.J. Benkovic, T.J. Huang, On-chip manipulation of single microparticles, cells, and organisms using surface acoustic waves, Proceedings of the National Academy of Sciences, 109 (2012) 11105-11109.
[9] X. Ding, P. Li, S.C. Lin, Z.S. Stratton, N. Nama, F. Guo, D. Slotcavage, X. Mao, J. Shi, F. Costanzo, T.J. Huang, Surface acoustic wave microfluidics, Lab on a Chip, 13 (2013) 3626-3649.
[10] A.A. Doinikov, P. Thibault, P. Marmottant, Acoustic streaming induced by two orthogonal ultrasound standing waves in a microfluidic channel, Ultrasonics, 87 (2018) 7-19.
[11] J. Nam, H. Lim, D. Kim, S. Shin, Separation of platelets from whole blood using standing surface acoustic waves in a microchannel, Lab on a Chip, 11 (2011) 3361-3364.
[12] Y. Chen, M. Wu, L. Ren, J. Liu, P.H. Whitley, L. Wang, T.J. Huang, High-throughput acoustic separation of platelets from whole blood, Lab on a Chip, 16 (2016) 3466-3472.
[13] X. Ding, Z. Peng, S.C. Lin, M. Geri, S. Li, P. Li, Y. Chen, M. Dao, S. Suresh, T.J. Huang, Cell separation using tilted-angle standing surface acoustic waves, Proc. Natl. Acad. Sci. USA, 111 (2014) 12992-12997.
[14] M. Wu, P.H. Huang, R. Zhang, Z. Mao, C. Chen, G. Kemeny, P. Li, A.V. Lee, R. Gyanchandani, A.J. Armstrong, Circulating Tumor Cell Phenotyping via High-Throughput Acoustic Separation, Small, 14 (2018) 1801131.
[15] D. Xu, F. Cai, M. Chen, F. Li, C. Wang, L. Meng, D. Xu, W. Wang, J. Wu, H. Zheng, Acoustic manipulation of particles in a cylindrical cavity: Theoretical and experimental study on the effects of boundary conditions, Ultrasonics, 93 (2019) 18-25.

[16] C. Sun, F. Wu, Y. Fu, D.J. Wallis, R. Mikhaylov, F. Yuan, D. Liang, Z. Xie, H. Wang, R. Tao, M.H. Shen, J. Yang, W. Xun, Z. Wu, Z. Yang, H. Cang, X. Yang, Thin film Gallium nitride (GaN) based acoustofluidic Tweezer: Modelling and microparticle manipulation, Ultrasonics, 108 (2020) 106202.
[17] P.B. Muller, R. Jensen, M. J. Bruus, H., A numerical study of microparticle acoustophoresis driven by acoustic radiation forces and streaming-induced drag forces, Lab on a Chip, 12 (2012) 4617-4627.
[18] N. Nama, R. Barnkob, Z. Mao, C.J. Kahler, F. Costanzo, T.J. Huang, Numerical study of acoustophoretic motion of particles in a PDMS microchannel driven by surface acoustic waves, Lab on a Chip, 15 (2015) 2700-2709.
[19] Z. Ni, C. Yin, G. Xu, L. Xie, J. Huang, S. Liu, J. Tu, X. Guo, D. Zhang, Modelling of SAW-PDMS acoustofluidics: physical fields and particle motions influenced by different descriptions of the PDMS domain, Lab on a Chip, 19 (2019) 2728-2740.
[20] N.R. Skov, P. Sehgal, B.J. Kirby, H. Bruus, Three-Dimensional Numerical Modeling of Surface-Acoustic-Wave Devices: Acoustophoresis of Micro- and Nanoparticles Including Streaming, Physical Review Applied, 12 (2019) 044028.
[21] J.-C. Hsu, C.-L. Chao, Full-wave modeling of micro-acoustofluidic devices driven by standing surface acoustic waves for microparticle acoustophoresis, Journal of Applied Physics, 128 (2020) 124502.
[22] R. Mikhaylov, F. Wu, H. Wang, A. Clayton, C. Sun, Z. Xie, D. Liang, Y. Dong, F. Yuan, D. Moschou, Z. Wu, M.H. Shen, J. Yang, Y. Fu, Z. Yang, C. Burton, R.J. Errington, M. Wiltshire, X. Yang, Development and characterisation of acoustofluidic devices using detachable electrodes made from PCB, Lab on a Chip, 20 (2020) 1807-1814.
[23] H. Bruus, Acoustofluidics 2: Perturbation theory and ultrasound resonance modes, Lab on a Chip, 12 (2012) 20-28.
[24] W.L. Nyborg, Acoustic streaming, in: W.P. Mason, R.N. Thurston (Eds.) Physical acoustics, Academic Press, New York, 1965, pp. 265–329.
[25] S. Shiokawa, Y. Matsui, T. Ueda, Study on SAW Streaming and its Application to Fluid Devices, Japanese Journal of Applied Physics, 29 (1990) 137-139.
[26] M. Settnes, H. Bruus, Forces acting on a small particle in an acoustical field in a viscous fluid, Phys Rev E Stat Nonlin Soft Matter Phys, 85 (2012) 016327.
[27] A. Shamloo, M. Boodaghi, Design and simulation of a microfluidic device for acoustic cell separation, Ultrasonics, 84 (2018) 234-243.
[28] C. Devendran, T. Albrecht, J. Brenker, T. Alan, A. Neild, The importance of travelling wave components in standing surface acoustic wave (SSAW) systems, Lab on a Chip, 16 (2016) 3756-3766.
[29] A.I. Viktorov, Rayleigh and lamb waves: physical theory and application, Plenum press, New York, 1967.
[30] J. Vanneste, O. Bühler, Streaming by leaky surface acoustic waves, Proceedings of The Royal Society A, 467 (2011) 1779-1800.
[31] J.K. Tsou, J. Liu, A.I. Barakat, M.F. Insana, Role of ultrasonic shear rate estimation errors in assessing inflammatory response and vascular risk,

Ultrasound in medicine & biology, 34 (2008) 963-972.
[32] Z. Mao, Acoustophoresis and fluid dynamics in surface acoustic wave-based acoustofluidics, Doctoral dissertation, The Pennsylvania State University, 2017.
[33] D. Köster, Numerical Simulation of Acoustic Streaming on SAW-driven Biochips, Doctoral dissertation, Universität Augsburg, Germany, 2006.
[34] M. Holmes, N. Parker, M. Povey, Temperature dependence of bulk viscosity in water using acoustic spectroscopy, in: Journal of Physics: Conference Series, IOP Publishing, 2011, pp. 012011.
[35] L.D. Landau, E.M. Lifshitz, A.M. Kosevich, J.B. Sykes, L.P. Pitaevskii, W.H. Reid, Theory of Elasticity: Volume 7, Elsevier Science, 1986.
[36] D. Armani, C. Liu, N. Aluru, Re-configurable fluid circuits by PDMS elastomer micromachining, in: Technical Digest. IEEE International MEMS 99 Conference. Twelfth IEEE International Conference on Micro Electro Mechanical Systems (Cat. No. 99CH36291), IEEE, 1999, pp. 222-227.
[37] C. Product, CRC Handbook of Chemistry and Physics, in: Taylor and Francis Group, 2012.
[38] L. Bergmann, Der ultraschall und seine anwendung in wissenschaft und technik, 6th ed., S. Hirzel Verlag, Stuttgart, 1954.